Photoionization of few electron systems: a hybrid coupled channels approach

You may also be interested in:

New Journal of Physics

The open access journal at the forefront of physics

CrossMark

PAPER

Photoionization of few electron systems: a hybrid coupled channels approach

Vinay Pramod Majety, Alejandro Zielinski and Armin Scrinzi

Physics Department, Ludwig Maximilians Universität, D-80333 Munich, Germany

E-mail: armin.scrinzi@lmu.de

Abstract

We present the hybrid anti-symmetrized coupled channels method for the calculation of fully differential photo-electron spectra of multi-electron atoms and small molecules interacting with strong laser fields. The method unites quantum chemical few-body electronic structure with strong-field dynamics by solving the time dependent Schrödinger equation in a fully anti-symmetrized basis composed of multi-electron states from quantum chemistry and a one-electron numerical basis. Photoelectron spectra are obtained via the time dependent surface flux (tSURFF) method. Performance and accuracy of the approach are demonstrated for spectra from the helium and beryllium atoms and the hydrogen molecule in linearly polarized laser fields at wavelengths from 21 to 400 nm. At long wavelengths, helium and the hydrogen molecule at equilibrium inter-nuclear distance can be approximated as single channel systems whereas beryllium needs a multi-channel description.

1. Introduction

Understanding laser-atom/molecule interaction has become an important research pursuit with the introduction of many versatile light probes over the past decade. Experimental techniques like re-collision imaging [1] and attosecond streaking [2] are being pursued to study time resolved electron dynamics. One of the factors that always creates a certain amount of vagueness in interpreting these strong field ionization experiments is the possible presence of multi-electron effects. An accurate interpretation of the experiments needs solutions of the multi-electron time dependent Schrödinger equation (TDSE). As perturbation theory is not valid in the strong field regime, one resorts to direct numerical solutions of the TDSE.

While simple single electron models or low dimensional models have been partially successful in explaining laser matter interactions, there have been several cases reported where a more elaborate description of electronic structure becomes important. Some of the examples include inter-channel coupling leading to an enhancement in high harmonic generation (HHG) from xenon [3], modification of angle resolved ionization yield of CO_2 [4] and photoionization cross-sections in SF_6 [5], enhancement in HHG due to participation of doubly excited states in beryllium [6], influence of nuclear motion [7], presence of conical intersections [8] and so on. All these instances need a more involved description of the electronic structure.

With one and two electron systems, a full dimensional numerical treatment is possible in linearly polarized laser fields. For systems with more than 6 degrees of freedom a full dimensional calculation is infeasible. There have been several efforts in the past decade to overcome this barrier of dimensionality for few electron systems by choosing only a part of the Hilbert space that is seemingly important for the dynamics. Some of the approaches that are being employed are time dependent configuration interaction methods [9], different variants of multi-configuration methods [10–17], the time-dependent R-matrix method [18], and coupled channel methods [4].

One of the observables that is typically measured in strong laser-atom/molecule interaction experiments are photoelectron spectra. While the methods listed above [4, 9–18] have tried to include multi-electron effects in photoionization studies, calculation of photoelectron spectra from multi-electron systems, especially at long

wavelengths has remained out of computational reach. The particular difficulty arises from the fact that, in order to compute photoelectron spectra the asymptotic part of the wavefunction is required. This needs large simulation box volumes and access to exact single continuum states to project the wavefunction onto at the end of time propagation. Having large simulation boxes and computing single continuum states of a multi-electron system are expensive tasks, making these kind of computations costly or outright impossible.

In this respect, a recently developed method called the time dependent surface flux (tSURFF) method [19, 20] has turned out to be an attractive solution. In the tSURFF approach, the wavefunction outside a certain simulation box is absorbed, and the electron flux through the box surface is used to obtain photoelectron spectra. This way photoelectron spectra can be computed with minimal box sizes.

We deal with the difficulties of the few body problem and computation of photoelectron spectra by combining quantum chemical structure with tSURFF for single electron systems through a coupled channels approach. The ansatz is similar in spirit to the one presented in [4]. However, unlike in [4], we deal with anti-symmetrization exactly. We discretize our multi-electron wavefunctions with the neutral ground state of the system and with anti-symmetrized products of the system's single ionic states and a numerical one-electron basis. This ansatz is suitable to study single ionization problems. The ionic and neutral states are computed by the COLUMBUS code [21] giving us the flexibility to treat the ionic states at various levels of quantum chemistry. While the fully flexible active electron basis describes the ionizing electron, the ionic basis describes the core polarization and the exact anti-symmetrization ensures indistinguishability of the electrons. The inclusion of the field-free neutral helps us to get the right ionization potential and start with the correct initial state correlation without much effort. We call our method hybrid fully anti-symmetrized coupled channels method and use the acronym haCC to refer to it in this work. Using tSURFF with haCC, we compute photoelectron spectra with minimal box sizes.

We intend to communicate in this article the mathematical formulation of our method, and demonstrate its usefulness by computing photoelectron spectra of He, H_2 and Be in linearly polarized 21–400 nm wavelength laser fields and compare them with fully numerical two electron results. We discuss the advantages and limitations of such an approach through suitable examples.

2. Mathematical formulation

In this section, we describe our mathematical setup to solve the N-electron TDSE in the presence of an external laser field. We solve

$$i\frac{\partial}{\partial t}\Psi = \hat{H}\Psi \tag{1}$$

with fixed nuclei approximation and with dipole approximation which implies neglecting the spatial dependence of the laser field. Atomic units $m_e = \hbar = e^2 = 1$ are used unless specified otherwise. The non-relativistic N-electron field-free Hamiltonian can be written as:

$$\hat{H} = \sum_i \left[-\frac{1}{2}\nabla_i^2 - \sum_p \frac{Z_p}{\left|\vec{r}_i - \vec{a}_p\right|} \right] + \sum_{i<j} \frac{1}{\left|\vec{r}_i - \vec{r}_j\right|}, \tag{2}$$

where Z_p is the nuclear charge and $\vec{a}_p$ are the nuclear coordinates of the pth nucleus. The interaction with the external laser field in length gauge is given by:

$$\hat{D}_L = -\sum_j \vec{E}(t) \cdot \vec{r}_j \tag{3}$$

and in velocity gauge by

$$\hat{D}_V = \sum_j i\vec{A}(t) \cdot \vec{\nabla}_j. \tag{4}$$

We describe our multi-electron discretization in detail in 2.1, present the time propagation equations in 2.2 and the matrix elements in 2.3. As the basis is non-orthogonal, an overlap matrix appears in the computation, whose efficient inversion by low rank updates will be presented in 2.4. Treating anti-symmetrization exactly and including neutrals introduces a technical difficulty in the form of linear dependencies in our basis. This is handled by performing a generalized inverse of the overlap matrix which will be presented in 2.5. We work in mixed gauge for the reasons detailed in [22] and briefed in 2.6. Finally, we present tSURFF for our coupled channels setup in section 2.7.

2.1. Multi-electron discretization

We discretize our *N*-electron wavefunction by channel wave functions chosen as anti-symmetrized products of ionic states with a numerical one-electron basis. To this we add the wave function of the neutral ground state, resulting in the expansion

$$|\Psi(t)\rangle \approx \sum_{\mathcal{I}} |\mathcal{I}\rangle C_{\mathcal{I}}(t) + |\mathcal{G}\rangle C_{\mathcal{G}}(t), \tag{5}$$

where

$$|\mathcal{I}\rangle = \mathcal{A}[|i\rangle|I\rangle]. \tag{6}$$

Here, $\mathcal{A}$ indicates anti-symmetrization, $|i\rangle$ are functions from a numerical one-electron basis, $|I\rangle$ and $|\mathcal{G}\rangle$ are (*N*-1) and *N* particle functions respectively and $C_{\mathcal{I}}(t)$, $C_{\mathcal{G}}(t)$ are the time dependent coefficients.

For the single electron basis $|i\rangle$ we use a finite element representation on the radial coordinate times spherical harmonics on the angular coordinates

$$|i(\vec{r})\rangle = |f_i(r)\rangle |Y_{l_i m_i}(\hat{r})\rangle. \tag{7}$$

On each finite element we use high order scaled Legendre polynomials as basis functions. The typical orders we use are 10–14. The details of the finite element approach used here can be found in [23, 24]. A brief description is given in appendix for the convenience of the reader. We refer to this basis as the active electron basis.

We choose $|I\rangle$ to be the eigenstates of the single ionic Hamiltonian obtained from the multi-reference configuration interaction singles doubles (MR-CISD) level of quantum chemistry. $|\mathcal{G}\rangle$ is chosen as the ground state of the system, also obtained from the MR-CISD level of quantum chemistry. These quantum chemistry wavefunctions are constructed with an atom centered primitive Gaussian basis as the starting point. While $|\mathcal{G}\rangle$ is the lowest eigenvector of the *N* particle Hamiltonian as obtained from COLUMBUS, it is not the ground state of the Hamiltonian in our basis: by treating one of the electrons with the active electron basis that is superior to the Gaussian basis one further improves the ground state energy.

The wavefunctions $|\mathcal{G}\rangle$ and $|I\rangle$ can be represented in a general form as sums of determinants:

$$|I\rangle = \sum_{p_1, p_2, ..., p_{n-1}} d_{p_1, p_2, ..., p_{n-1}} \left| \mathcal{A}\left[\phi_{p_1} \phi_{p_2} \cdots \phi_{p_{n-1}} \right] \right\rangle \tag{8}$$

$$|\mathcal{G}\rangle = \sum_{p_1, p_2, ..., p_n} d_{p_1, p_2, ..., p_n} \left| \mathcal{A}\left[\phi_{p_1} \phi_{p_2} \cdots \phi_{p_n} \right] \right\rangle, \tag{9}$$

where ϕ_k are the Hartree–Fock orbitals of the neutral system. The same set of Hartree–Fock orbitals are used to construct both ionic and neutral CI functions. This allows us to use simple Slater–Condon rules to compute any matrix elements between them.

The explicit inclusion of the neutral ground state is motivated by the fact that, while the ionization process itself may be well described by one or a few ionic channels, the initial ground state may be more strongly correlated. In order to avoid inclusion of many ionic states just to describe the initial state, we include the neutral ground state explicitly, thereby reducing the number of basis functions needed. This idea can be easily extended to include any specific correlated state that is of importance to a particular process.

2.2. Time propagation equations

Substituting the ansatz (5) into the TDSE (1) yields a set of coupled ordinary differential equations for the time dependent coefficients:

$$i\left[\langle \mathcal{G}|\mathcal{G}\rangle \frac{dC_{\mathcal{G}}}{dt} + \langle \mathcal{G}|\mathcal{I}\rangle \frac{dC_{\mathcal{I}}}{dt} \right] = \langle \mathcal{G}| \hat{H} |\mathcal{G}\rangle C_{\mathcal{G}} + \langle \mathcal{G}| \hat{H} |\mathcal{I}\rangle C_{\mathcal{I}} \tag{10}$$

$$i\left[\langle \mathcal{I}|\mathcal{G}\rangle \frac{dC_{\mathcal{G}}}{dt} + \langle \mathcal{I}|\mathcal{I}\rangle \frac{dC_{\mathcal{I}}}{dt} \right] = \langle \mathcal{I}| \hat{H} |\mathcal{G}\rangle C_{\mathcal{G}} + \langle \mathcal{I}| \hat{H} |\mathcal{I}\rangle C_{\mathcal{I}}. \tag{11}$$

The time-derivative of the coefficient vector is multiplied by an overlap matrix composed of the blocks $\langle \mathcal{G}|\mathcal{G}\rangle$, $\langle \mathcal{G}|\mathcal{I}\rangle$, $\langle \mathcal{I}|\mathcal{G}\rangle$ and $\langle \mathcal{I}|\mathcal{I}\rangle$.

We time propagate the coefficients using an explicit fourth order Runge–Kutta method with adaptive step size. In order to absorb the wavefunction at the box boundaries we use infinite range exterior complex scaling (irECS) [23]. We typically choose simulation boxes larger than the spatial extent of the Hartree–Fock orbitals and start absorption after the Hartree–Fock orbitals vanish. This implies that it suffices to complex scale only one of the *N* coordinates.

The cost of time propagation scales with the number of ionic states (say n_I) as n_I^2 and it is independent of the exact number of electrons. This makes basis sets of the kind (5) attractive for treating many electron systems.

2.3. Matrix elements

In order to solve the TDSE we need to evaluate various operators. Firstly, we introduce several generalized reduced density matrices with the help of creation $(a_k^\dagger)$ and annihilation (a_k) operators on the single particle state ϕ_k. A pth order generalized reduced density matrix between the $(N-1)$ particle ionic functions is given by:

$$\rho^{IJ}_{k_1,\ldots,k_p,l_1,\ldots,l_p} = \langle I| \, a_{k_1}^\dagger \ldots a_{k_p}^\dagger a_{l_1} \ldots a_{l_p} \, |J\rangle. \tag{12}$$

Similarly, we define generalized Dyson coefficients between the N-particle neutral wavefunctions and $(N-1)$ particle ionic wavefunctions as

$$\eta^{\mathcal{G}J}_{k_1,\ldots,k_p,l_1,\ldots,l_{p-1}} = \langle \mathcal{G}| \, a_{k_1}^\dagger \ldots a_{k_p}^\dagger a_{l_1} \ldots a_{l_{p-1}} \, |J\rangle. \tag{13}$$

With the help of these objects, we can present the final form of the matrix elements. The overlap matrix blocks have the form

$$\begin{aligned}
\langle \mathcal{G}|\mathcal{G}\rangle &= 1 \\
\langle \mathcal{G}|\mathcal{I}\rangle &= \eta^{\mathcal{G}I}_k \langle \phi_k|i\rangle \\
\langle \mathcal{I}|\mathcal{J}\rangle &= \langle i|j\rangle\langle I|J\rangle - \langle i|\phi_l\rangle\rho^{IJ}_{kl}\langle \phi_k|j\rangle \\
&= \langle i|j\rangle\delta_{IJ} - \langle i|\phi_l\rangle\rho^{IJ}_{kl}\langle \phi_k|j\rangle,
\end{aligned} \tag{14}$$

where $\eta^{\mathcal{G}I}_k$ can be identified with the Dyson orbital coefficients with respect to the Hartree–Fock orbitals and ρ^{IJ}_{kl} are the one particle reduced density matrices.

Any exchange-symmetric single particle operator can be written as

$$\hat{T} = \hat{t}(1) + \hat{t}(2) + \ldots + \hat{t}(N), \tag{15}$$

where $\hat{t}(u)$ is the single particle operator corresponding to the coordinate u. Matrix elements of $\hat{T}$ are

$$\begin{aligned}
\langle \mathcal{G}| \, \hat{T} \, |\mathcal{G}\rangle &= \rho^{\mathcal{G}\mathcal{G}}_{kl}\langle \phi_k| \, \hat{t} \, |\phi_l\rangle \\
\langle \mathcal{G}| \, \hat{T} \, |\mathcal{I}\rangle &= \eta^{\mathcal{G}I}_k\langle \phi_k| \, \hat{t} \, |i\rangle + \eta^{\mathcal{G}I}_{klm}\langle \phi_k| \, \hat{t} \, |\phi_m\rangle\langle \phi_l|i\rangle \\
\langle \mathcal{I}| \, \hat{T} \, |\mathcal{J}\rangle &= \langle i|j\rangle\langle I| \, \hat{t} \, |J\rangle + \langle i| \, \hat{t} \, |j\rangle\langle I|J\rangle - \langle i| \, \hat{t} \, |\phi_l\rangle\rho^{IJ}_{kl}\langle \phi_k|j\rangle \\
&\quad - \langle i|\phi_l\rangle\rho^{IJ}_{kl}\langle \phi_k| \, \hat{t} \, |j\rangle - \langle i|\phi_c\rangle\langle \phi_a|j\rangle\langle \phi_b| \, \hat{t} \, |\phi_d\rangle\rho^{IJ}_{abcd},
\end{aligned} \tag{16}$$

where $\eta^{\mathcal{G}I}_{klm}$ are the three index generalized Dyson coefficients, equation (13), and ρ^{IJ}_{abcd} are the two particle reduced density matrices, equation (12).

Finally, the two particle operators

$$\hat{V}^{(2)} = \sum_{i<j}\hat{v}(ij) \tag{17}$$

have the matrix elements

$$\langle \mathcal{G}| \, \hat{V}^{(2)} \, |\mathcal{G}\rangle = \frac{1}{2}\rho^{\mathcal{G}\mathcal{G}}_{abcd}\langle \phi_a\phi_b| \, \hat{v} \, |\phi_c\phi_d\rangle$$

$$\langle \mathcal{G}| \, \hat{V}^{(2)} \, |\mathcal{I}\rangle = \eta^{\mathcal{G}I}_{klm}\langle \phi_k\phi_l| \, \hat{v} \, |\phi_m i\rangle + \frac{1}{2}\eta^{\mathcal{G}I}_{abcde}\langle \phi_a\phi_b| \, \hat{v} \, |\phi_d\phi_e\rangle\langle \phi_c|i\rangle$$

$$\langle \mathcal{I}| \, \hat{V}^{(2)} \, |\mathcal{J}\rangle = \frac{1}{2}\rho^{IJ}_{abcd}\langle \phi_a\phi_b| \, \hat{v} \, |\phi_c\phi_d\rangle\langle i|j\rangle + \underbrace{\rho^{IJ}_{kl}\langle \phi_k i| \, \hat{v} \, |\phi_l j\rangle}_{\text{Direct term}} - \underbrace{\rho^{IJ}_{kl}\langle \phi_k i| \, \hat{v} \, |j\phi_l\rangle}_{\text{Standard exchange term}}$$

$$\underbrace{- \rho^{IJ}_{abcd}\langle \phi_a i| \, \hat{v} \, |\phi_c\phi_d\rangle\langle \phi_b|j\rangle - \rho^{IJ}_{abcd}\langle \phi_a\phi_b| \, \hat{v} \, |\phi_c j\rangle\langle i|\phi_d\rangle - \frac{1}{2}\rho^{IJ}_{abcdef}\langle \phi_a\phi_b| \, \hat{v} \, |\phi_d\phi_e\rangle\langle i|\phi_f\rangle\langle \phi_c|j\rangle}_{\text{Other exchange terms due to non-orthogonality}}, \tag{18}$$

where $\eta^{\mathcal{G}I}_{abcde}$ are the five index generalized Dyson coefficients, equation (13) and ρ^{IJ}_{abcdef} are the three particle reduced density matrices, equation (12). Although it appears from equation (18) that the necessity of ρ^{IJ}_{abcdef}, $\eta^{\mathcal{G}I}_{abcde}$ leads to large memory requirements, we must point out that the contractions $\rho^{IJ}_{abcdef}\langle \phi_a\phi_b|\hat{v}|\phi_d\phi_e\rangle$ and $\eta^{\mathcal{G}I}_{abcde}\langle \phi_a\phi_b|\hat{v}|\phi_d\phi_e\rangle$ can be made while computing ρ^{IJ}_{abcdef} and $\eta^{\mathcal{G}I}_{abcde}$ itself, thereby storing only simple matrices and vectors.

In order to compute the two-electron integrals, we first project the Hartree–Fock orbitals onto a single center expansion:

$$\phi_k(\vec{r}) = \sum_{q_k l_k m_k} d_{q_k l_k m_k} Y_{l_k m_k}(\theta, \phi), \tag{19}$$

where q_k are radial quadrature points, l_k, m_k refer to the angular momentum functions and use these expansions with the multi-pole expansion:

$$\frac{1}{|\vec{r_1} - \vec{r_2}|} = \sum_{LM} \frac{4\pi}{2L+1} \frac{r_<^L}{r_>^{L+1}} Y_{LM}(\theta_1, \phi_1) Y_{LM}^*(\theta_2, \phi_2) \tag{20}$$

with $r_< = \min(r_1, r_2)$ and $r_> = \max(r_1, r_2)$. The limits for the multi-pole expansion are determined by the angular momenta in the one-electron numerical basis and the single center expansion for the molecular orbitals ϕ_k. No other truncation schemes are employed. These two particle operators pose a challenge for efficient computation. While the direct term is relatively easy to handle, the exchange terms consume a major portion of the Hamiltonian setup time.

2.4. Inverse of the overlap matrix

The overlap matrix (14) is not a standard finite element overlap matrix, which would be banded and would allow for efficient application of the inverse. Rather, non-orthogonality between the active electron basis and the Hartree–Fock orbitals leads to extra cross terms that destroy the banded structure in general and complicate the computation of the inverse. However, the inverse of the overlap can still be computed efficiently using low rank updates. We use here the Woodbury formula [25], according to which the inverse of a modified matrix of the form $(S_0 - U\Lambda U^\dagger)$ can be computed as:

$$\begin{aligned} S^{-1} &= (S_0 - U\Lambda U^\dagger)^{-1} \\ &= S_0^{-1} - S_0^{-1} U (U^\dagger S_0^{-1} U - \Lambda^{-1})^{-1} U^\dagger S_0^{-1}. \end{aligned} \tag{21}$$

As an example, with 2 ionic states and 1 neutral the overlap matrix (14) can be cast in the form:

$$S = \underbrace{\begin{pmatrix} s_0 & 0 & 0 \\ 0 & s_0 & 0 \\ 0 & 0 & 1 \end{pmatrix}}_{S_0} - \underbrace{\begin{pmatrix} u & 0 & 0 \\ 0 & u & 0 \\ 0 & 0 & 1 \end{pmatrix}}_{U} \underbrace{\begin{pmatrix} \rho^{11} & \rho^{12} & \eta^{G1} \\ \rho^{21} & \rho^{22} & \eta^{G2} \\ [\eta^{G1}]^T & [\eta^{G2}]^T & 0 \end{pmatrix}}_{\Lambda} U^\dagger \tag{22}$$

which is suitable for the Woodbury formula (21). Here, $(s_0)_{ij} = \langle i|j\rangle$ and $u_{ik} = \langle i|\phi_k\rangle$. Let n_a denote the number of active electron basis functions $|i\rangle$ and n_{hf} be the number of Hartree–Fock orbitals ϕ_k that is much smaller that n_a. The overlap matrix s_0 has dimensions $n_a \times n_a$ but is narrowly banded, and the dimensions of matrix u are $n_a \times n_{hf}$.

Let n_I be the number of ionic states. Then the overlap S and S_0 are $(n_I n_a + 1) \times (n_I n_a + 1)$ matrices, where the inverse of S_0 can be easily applied. The matrix U is $(n_I n_a + 1) \times (n_I n_{hf} + 1)$ and Λ is $(n_I n_{hf} + 1) \times (n_I n_{hf} + 1)$. This low rank structure of the correction terms can be utilized to compute the inverse efficiently by using the Woodbury formula.

2.5. Handling linear dependencies

Anti-symmetrization and non-orthogonality of the active electron basis with respect to the Hartree–Fock orbitals may render our basis linearly dependent. If the $\{|i\rangle\}$-basis is near-complete w.r.t. the HF-orbital basis

$$\langle\phi_k|i\rangle \, [s_0^{-1}]_{ij} \, \langle j|\phi_l\rangle \approx \delta_{kl}, \tag{23}$$

it is possible to find coefficients $c_{i,I}$ such that

$$\sum_{i,I} c_{i,I} \mathcal{A}[|i\rangle|I\rangle] \approx 0. \tag{24}$$

An obvious case where this happens is when one and the same HF orbital ϕ_{k_0} appears in all the ionic determinants. For a linear combination $\sum_i c_{i,I}|i\rangle \approx \phi_{k_0}$ anti-symmetrization renders equation (24) near zero. As a result, the overlap matrix becomes non-invertible. A possible solution would be to orthogonalize the active electron basis with respect to the Hartree–Fock orbitals. But this is not an easily implementable solution with a CI ionic basis. For each determinant, the set of Hartree–Fock orbitals with respect to which the active electron basis must be orthogonal is different.

As an alternative solution we use a generalization of the Woodbury formula (21) to compute the inverse of a matrix only on the subspace of the non-zero eigenvectors of the matrix. Let Z denote the $n_0 \times n_z$ matrix of eigenvectors with near-zero eigenvalues $z_p < \epsilon$, $p = 1, \ldots, n_z$ of the generalized eigenvalue problem

$$SZ = S_0 Z d_z, \tag{25}$$

with d_z denoting the diagonal matrix of the eigenvalues z_p and Z satisfying the orthonormality relation $Z^\dagger S_0 Z = \mathbf{1}$. In general, there will be comparatively few such eigenvectors $n_z \ll n_0$ and these can be easily determined by an iterative solver. We can remove these singular vectors from our calculation by the projector

$$Q = 1 - Z Z^\dagger S_0. \tag{26}$$

The projector property $Q^2 = Q$ can be easily verified. As the projector refers to the generalized eigenvalue problem with $S_0 \neq \mathbf{1}$, Q is not an orthogonal projector, that is $Q^\dagger \neq Q$. We define a pseudo-inverse $\tilde{S}^{-1}$ of S on the subspace of generalized eigenvectors with non-zero eigenvalues with the property

$$\tilde{S}^{-1} S Q = Q. \tag{27}$$

One can verify directly that the generalized Woodbury formula

$$\tilde{S}^{-1} = Q S_0^{-1} \left[1 - U \left(U^\dagger Q S_0^{-1} U - \Lambda \right)^{-1} U^\dagger Q S_0^{-1} \right] \tag{28}$$

satisfies the definition (27). The matrix $(U^\dagger Q S_0^{-1} U - \Lambda)$ is invertible on all vectors appearing in $U^\dagger Q$ to its right, as exactly the singular vectors are removed by the projector Q. Apart from the necessity to determine Z during setup, the correction does not significantly increase the operations count for the inverse overlap.

2.6. Choice of gauge

In [22], we had shown that when an electron is treated with a restricted basis, for example, in terms of a few bound states, the length gauge is a more natural gauge. Compared to pure velocity gauge, the coupled channel computations converge quickly in mixed gauge with length gauge spanning the region of the ionic states and velocity gauge thereafter for asymptotics. In this current work, we use continuous gauge switching, detailed in [22], for its easy implementation. Starting from the length-gauge, we solve the TDSE after applying the gauge transformation

$$U_c = \begin{cases} 1 & \text{for } r \leqslant r_\mathrm{g}, \\ \exp\left[\mathrm{i} \vec{A}(t) \cdot \sum_{j=1}^{N} \hat{r}_j (r_j - r_\mathrm{g}) \right] & \text{for } r > r_\mathrm{g}. \end{cases} \tag{29}$$

Here, r_g is the gauge radius that separates the length gauge and velocity gauge regions.

2.7. Computation of photoelectron spectra

The computation of photoelectron spectra is expensive for two reasons. (1) The asymptotic part of the wavefunction is needed to extract photoelectron spectra, which means large simulation boxes to preserve the asymptotic part and to avoid any numerical reflections that may corrupt the wavefunction. (2) Single continuum states are needed into which the wavefunction must be decomposed, in order to obtain photoelectron spectra. These two problems are circumvented in a recently developed method tSURFF [19, 20]: one computes the spectra by a time integration of electron flux through a surface defined by a radius R_c called the tSURFF radius. The Coulomb potential is smoothly turned off before R_c, which implies that the scattering solutions thereafter are the well known Volkov solutions. R_c becomes a convergence parameter, and by varying this radius, one can compute spectra to a given accuracy. This method has been explained in detail in previous works for single ionization in [19] and for double ionization in [20]. A proposal for extension of this method for single ionization of multi-electron systems has been outlined in [20]. We describe here the application of the method with our coupled channels setup.

Let χ_k be the scattering solutions which take the form of Volkov solutions beyond R_c and $\Psi(T)$ be the wavefunction at some large time T. According to tSURFF for single electron systems, photoelectron spectra can be computed as $\sigma_k = |b_k|^2$ with b_k defined as:

$$\begin{aligned} b_k &= \left\langle \chi_k(T) \middle| \Theta(R_c) \middle| \Psi(T) \right\rangle \\ &= \mathrm{i} \int_0^T \mathrm{d}t \left\langle \chi_k(t) \middle| \left[-\frac{1}{2}\triangle + \mathrm{i}\vec{A}(t) \cdot \vec{V}, \Theta(R_c) \right] \middle| \Psi(t) \right\rangle. \end{aligned} \tag{30}$$

Here $\Theta(R_c)$ is a Heaviside function that is unity for $r > R_c$ and 0 elsewhere.

This formulation can be easily extended to the N electron problem in a coupled channels setup. In the present setup, we mostly take a set of ionic bound states for the ionic basis. These states have a finite extent. We may choose R_c such that the electrons described by the ionic basis vanish by R_c which means all the exchange terms in the Hamiltonian vanish after R_c. The remaining direct potential can be smoothly turned off just as the Coulomb potential. This implies that the wavefunction beyond R_c evolves by the Hamiltonian:

$$H(r > R_c) = H_{\text{ion}} \otimes \hat{1} + \hat{1}_{\text{ion}} \otimes \left[-\frac{1}{2} \triangle + i\vec{A}(t) \cdot \vec{\nabla} \right] \tag{31}$$

that allows for a complete set of solutions of the form:

$$\xi_{c,k}(\vec{r}_1, \ldots, \vec{r}_n, t) = \mathcal{A}\left[\kappa_c(\vec{r}_1, \ldots, \vec{r}_{n-1}, t) \otimes \chi_k(\vec{r}_n, t) \right], \tag{32}$$

where H_{ion} is the single ionic Hamiltonian and $\kappa_c(t)$ are time dependent ionic channel functions solving the TDSE

$$i\frac{\partial \kappa_c(t)}{\partial t} = \hat{H}_{\text{ion}} \kappa_c(t) \tag{33}$$

within the ansatz in terms of field-free ionic states

$$|\kappa_c(t)\rangle = \sum_I |I\rangle d_{cI}(t). \tag{34}$$

With the help of the $\xi_{c,k}$, channel resolved photoelectron spectra can be computed as

$$\sigma_{c,k} = \left| \left\langle \xi_{c,k}(\vec{r}_1, \ldots, \vec{r}_n, T) \right| \Theta(R_c) | \Psi(\vec{r}_1, \ldots, \vec{r}_n, T) \rangle \right|^2 \tag{35}$$

and the asymptotic decomposition of Ψ in terms of $\xi_{c,k}$ is obtained as

$$\left\langle \xi_{c,k}(\vec{r}_1, \ldots, \vec{r}_n, T) \right| \Theta(R_c) | \Psi(\vec{r}_1, \ldots, \vec{r}_n, T) \rangle$$
$$= i \int_0^T dt \left\langle \mathcal{A}\left[\kappa_c(\vec{r}_1, \ldots, \vec{r}_{n-1}, t) \otimes \chi_k(\vec{r}_n, t) \right] \right| \left[-\frac{1}{2}\triangle_n + i\vec{A}(t) \cdot \vec{\nabla}_n, \Theta_n(R_c) \right] | \Psi(\vec{r}_1, \ldots, \vec{r}_n, t) \rangle$$
$$= i \int_0^T dt \left\langle \chi_k(\vec{r}_n, t) \right| \left[-\frac{1}{2}\triangle_n + i\vec{A}(t) \cdot \vec{\nabla}_n, \Theta_n(R_c) \right] | \zeta_c(\vec{r}_n, t) \rangle, \tag{36}$$

where we introduced the time-dependent Dyson orbitals

$$\zeta_c(\vec{r}_n, t) := \langle \kappa_c(\vec{r}_1, \ldots, \vec{r}_{n-1}, t) | \Psi(\vec{r}_1, \ldots, \vec{r}_n, t) \rangle. \tag{37}$$

The commutator of the derivatives with the Heaviside function Θ gives δ-like terms involving values and derivatives of Ψ at the surface $|\vec{r}| = R_c$. As we choose R_c such that the Hartree–Fock orbitals vanish by then, we do not need to consider the exchange terms in computing ζ_c. Along with time propagating the N electron problem, one needs to also time propagate the ionic problem (33).

A detailed discussion of performance and intrinsic limitations of the tSURFF method is contained in [19, 20]. We here summarize the main points of this discussion. The strength of tSURFF lies (a) in a dramatic reduction of the required numerical box sizes to compute accurate spectra and (b) in the fact that no scattering states are needed for spectral analysis. As the asymptotic scattering information is generated during time-propagation rather than by solving an independent stationary problem, propagation times must be long enough for all relevant processes to terminate and for all electrons to pass through the surface. This favors the application of the method for fast processes. For slow processes like emission at near zero electron energy or the decay of long-lived resonances purely stationary methods or methods that combine solutions of the TDSE during pulse with a stationary analysis after the end of the pulse may become advantageous. Also, if small boxes are used, the capability for representing very extended objects like Rydberg states is limited by the box size. We will illustrate these points below when discussing photo-emission from the helium atom at short wave length.

2.8. Spin symmetry
As we solve the non-relativistic TDSE, the total spin of the system is conserved during the time evolution. We can therefore remove the spin degree of freedom through suitable linear combinations of the anti-symmetrized products in the basis (5) to enforce a particular spin symmetry. This reduces the size of our basis. We consider only singlet spin symmetric systems in this work. As an example, we show how singlet spin symmetry can be enforced. Let ↑ and ↓ indicate the spin states $\pm\frac{1}{2}$ associated with a spatial function. Choosing linear combinations of the kind:

$$\mathcal{A}[|I\rangle|i\rangle] := \frac{\mathcal{A}\left[|I^{\uparrow}\rangle|i^{\downarrow}\rangle\right] - \mathcal{A}\left[|I^{\downarrow}\rangle|i^{\uparrow}\rangle\right]}{\sqrt{2}} \tag{38}$$

enforces singlet symmetry. This can be extended to creating linear combinations that enforce an arbitrary spin symmetry.

3. Two-electron benchmark calculations

We use two-electron full dimensional calculations (full-2e) as benchmark for our haCC computations. We solve the two-electron TDSE using an independent particle basis of the form:

$$\Psi(\vec{r}_1, \vec{r}_2, t) = \sum_{k_1 k_2 l_1 l_2 m} c_{k_1 k_2 l_1 l_2 m}(t) f_{k_1}(r_1) f_{k_2}(r_2) Y_{l_1 m}(\theta_1, \phi_1) Y_{l_2 -m}(\theta_2, \phi_2),$$ (39)

where $c_{k_1 k_2 l_1 l_2 m}(t)$ are the time dependent coefficients, $f_{k_1}(r_1)$, $f_{k_2}(r_2)$ are functions from a finite element discretization of the same type as for our active electron basis and Y_{lm} are spherical harmonics. We use the same type of single center expansion for all the benchmark computations. A complete description of this method will be presented elsewhere [24]. Solving the TDSE with the expansion (39) needs much larger computational resources compared to the haCC approach.

The purpose of the two-electron calculations is to demonstrate to which extent these fully correlated calculations are reproduced by the haCC approach. For that we use the same tSURFF propagation times and identical box sizes when comparing the two types of calculations. Full convergence of the two-electron calculation in propagation time and box size is not discussed in the present paper.

4. Single photoelectron spectra

In this section, we present photoelectron spectra from helium and beryllium atoms and from the hydrogen molecule with linearly polarized laser fields computed with the above described coupled channels formalism. We also present the single photon ionization cross-sections for the beryllium atom and the wavelength dependence of the ionization yield for the hydrogen molecule to compare with other existing calculations. We use $\cos^2$ envelope pulses for all the calculations and the exact pulse shape is given as

$$A_z(t) = A_0 \cos^2\left(\frac{\pi t}{2cT}\right) \sin\left(\frac{2\pi t}{T} + \beta\right)$$ (40)

$$E_z(t) = -\frac{\mathrm{d}A_z(t)}{\mathrm{d}t},$$ (41)

where T is the single cycle duration, $A_0 = E_0 T/(2\pi)$ for a peak field strength E_0, c is the number of laser cycles and β is the carrier envelope phase. We compare our results for helium and the hydrogen molecule with full-2e calculations [24] and for beryllium with effective two electron model calculations.

The convergence of the full-2e benchmark calculations and the haCC calculations were done systematically and independently. All the spectra presented here were computed with simulation box sizes on the scale of $R_c \sim 30–50$ a.u. The radial finite element basis consisted of high order polynomials with typical orders 10–14 and the total number of radial basis functions was such that there were 2–3 functions per atomic unit. The angular momenta requirement strongly depends on the wavelength. The longer wavelengths needed larger number of angular momenta for convergence. For the examples considered below, the angular momenta range from $L_{\max} = 5$ at 21 nm to $L_{\max} = 30$ at 400 nm. All the calculations presented are converged with respect to the single electron basis parameters like the order and the box size, well below the differences caused by inclusion of ionic states. Hence, we only present various observables as a function of the number of ionic states.

The storage requirements with the algorithms that we use are dictated by the two particle reduced density matrices. For the largest problem considered here, with 11 ionic states (n_I) and about 50 molecular orbitals (n_{hf}), the number of doubles that had to be stored is given by the formula: $\dfrac{n_I(n_I + 1)}{2} \dfrac{n_{hf}^2(n_{hf} + 1)^2}{4}$, which yields a storage requirement of 1.7 GB. This is not a large requirement in the context of the currently available computational resources. In order to avoid replication, these objects were stored in shared memory. The computation times vary widely depending on the wavelength and the number of ionic states in the basis. They scale with the square of the number of ionic states. For the cases presented here, the required times range from 0.25–30 h on an eight core machine. These times also have a strong dependence on the exact time propagators used and a discussion on the suitable time propagators is out of the scope of this work.

4.1. Helium

Helium is the largest atom that can be numerically treated in full dimensionality. With linearly polarized laser fields, the symmetry of the system can be used to reduce the problem to five-dimensions. The energies of the helium ionic states are $-2/n^2$ for principal quantum number n. The first two ionic states are separated by 1.5 a.u. in energy, which is large, for example, compared to a photon energy of 0.456 a.u. at 100 nm. This has been a motivation to treat helium as an effective single electron system with XUV and longer wavelengths in some
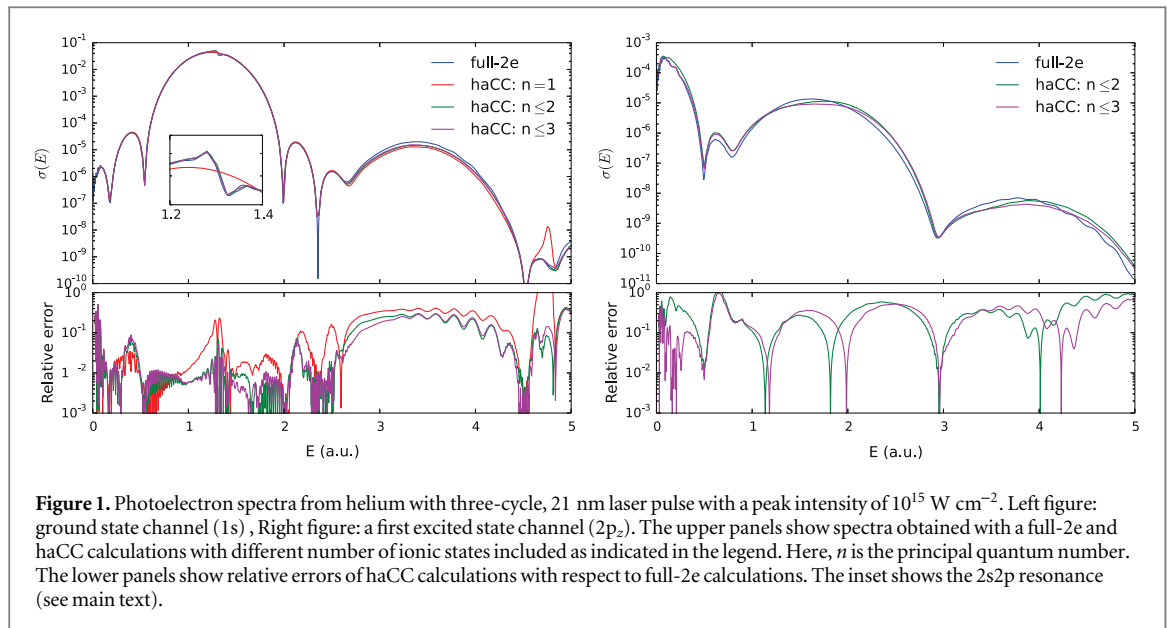
Figure 1. Photoelectron spectra from helium with three-cycle, 21 nm laser pulse with a peak intensity of 10^{15} W cm^{-2}. Left figure: ground state channel (1s), Right figure: a first excited state channel ($2p_z$). The upper panels show spectra obtained with a full-2e and haCC calculations with different number of ionic states included as indicated in the legend. Here, n is the principal quantum number. The lower panels show relative errors of haCC calculations with respect to full-2e calculations. The inset shows the 2s2p resonance (see main text).

earlier works, for example in [26]. We examine below the validity of treating helium as an effective single electron system, by comparing haCC calculations with full dimensional calculations at different wavelengths.
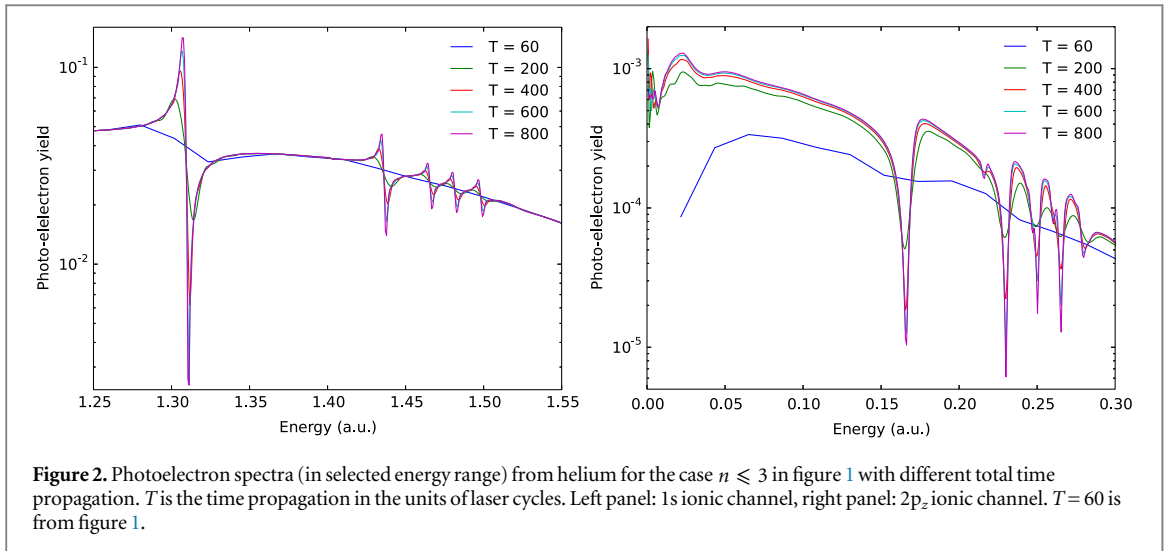
Figure 1 shows photoelectron spectra from helium with a 21 nm ($\omega = 2.174$ a.u.), three cycle laser pulse with a peak intensity of 10^{15} W cm^{-2}. The one and two photon ionization peaks of 1s and $2p_z$ channel spectra are shown. The relative errors of haCC calculations are computed with respect to the full dimensional calculation. The single photon peak of the 1s channel is computed to a few percent accuracy, except for a feature around 1.3 a.u., with a single ionic state. The resonant feature can be identified with the 2s2p doubly excited state [27], which is reproduced to few percent accuracy with the addition of 2nd shell ionic states. While the position of the resonance is reproduced accurately in the calculations presented here, the propagation time was well below the life-time of this resonance which is reflected in the width of the feature that is well above the natural line width.

The two photon peak of the 1s channel and the $2p_z$ channel spectra (figure 1) need more than a single ionic state and they could be computed only up to 15% accuracy even after inclusion of 9 ionic states ($n \leqslant 3$).

A broadband (few cycle) XUV pulse tends to excite the initial state into a band of final states which may include many correlated intermediate states. Here, the intrinsic limitations of any coupled channels approach that is based on ionic bound states only are exposed. Firstly, a correlated intermediate state with a bound character needs large number of ionic states to be correctly represented. Secondly, the ionic bound states based on Gaussian basis sets do not have the exact asymptotic behavior. This can lead to an inaccuracy in length gauge dipole matrix elements. Finally, the absence of ionic continuum states in our approach is another possible source of inaccuracy. Due to these limitations, we do not expect the shake-up channel spectra to be more accurate than 10–15%.

For obtaining long-lived resonance structures by a time-dependent method one must, as a general feature of such methods, propagate for times at least on the scale of the life time of the resonance. The only alternative is to independently solve the stationary resonant scattering problem and decompose the time-dependent solution after the end of the pulse into the corresponding scattering continuum. Solving the scattering problem, however, is a computationally very demanding task by itself. For obtaining the resonances with tSURFF, one can simply propagate until the resonance has decayed completely and all flux has passed through the surface where the flux is collected. At this point it should be remarked that the relevant information about resonances may be generated more efficiently by stationary methods like time-independent complex scaling [27, 28]. As the comparison in figure 1 is with the two-electron code where long propagation times become rather costly, we compare the spectra at time $T = 60$ laser cycles, where the resonances have not emerged yet.

With haCC, due to its very compact representation, we can easily propagated much longer to obtain the resonances to any desired accuracy. Figure 2 shows how the $n \leqslant 3$ resonances emerge with increasing propagation times in the 1s and $2p_z$ channels. For example, at the 2s2p decay width of $\Gamma = 1.37 \times 10^{-3}$, one expects 76.5% of the Auger electrons to have passed through the surface $|\vec{r}| = 45$ at time $T = 400$, which increases to 95.2% at $T = 800$. The ratio of 1.24 between these numbers closely matches the increase of mass in the 2s2p peak by 1.23 in figure 2. The positions of the resonances are accurate on the level of 10^{-3} a.u. in energy [27], showing that the correlated states are well represented by the method. Here we had chosen a box size of 45 a.u. which is sufficient to represent doubly excited states from 2s2p to 2s6p states. Hence, only these states are

Figure 2. Photoelectron spectra (in selected energy range) from helium for the case $n \leqslant 3$ in figure 1 with different total time propagation. *T* is the time propagation in the units of laser cycles. Left panel: 1s ionic channel, right panel: $2p_z$ ionic channel. $T = 60$ is from figure 1.
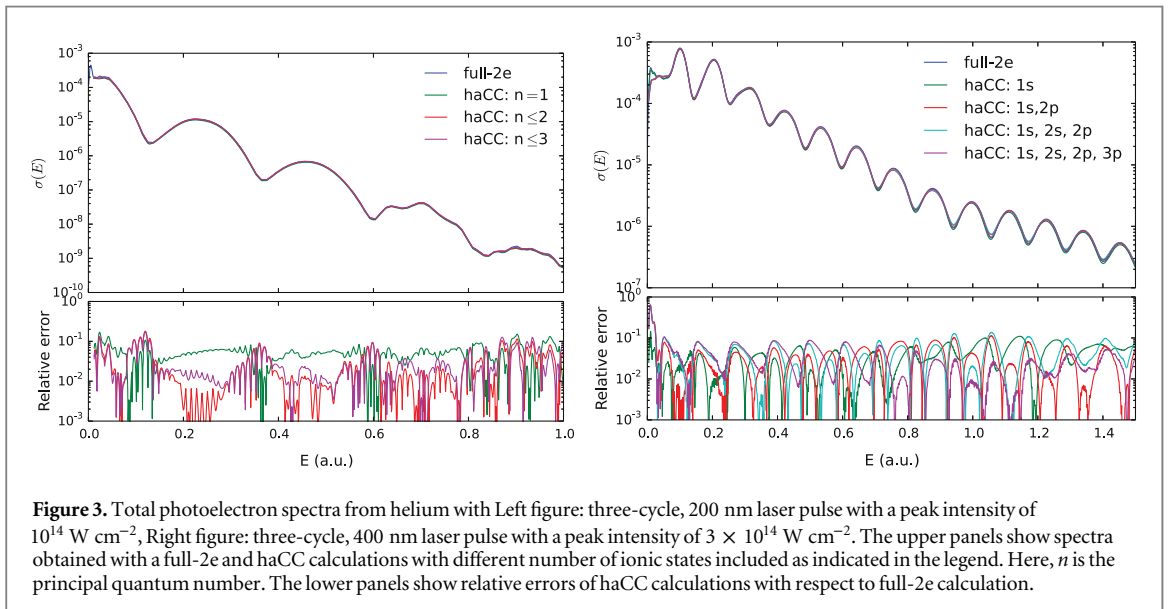
Figure 3. Total photoelectron spectra from helium with Left figure: three-cycle, 200 nm laser pulse with a peak intensity of 10^{14} W cm^{-2}, Right figure: three-cycle, 400 nm laser pulse with a peak intensity of 3×10^{14} W cm^{-2}. The upper panels show spectra obtained with a full-2e and haCC calculations with different number of ionic states included as indicated in the legend. Here, *n* is the principal quantum number. The lower panels show relative errors of haCC calculations with respect to full-2e calculation.

seen in the spectra. One can obtain the higher excited states by increasing the box size, at the penalty of a larger discretization and somewhat longer propagation times, see discussion in section 2.7. Similar as long lived resonances, threshold behavior of the spectrum near energy zero only emerges with propagation time, figure 2. Further distortions near threshold are due to the effective truncation of the Coulomb tail in the absorbing region. In the present example, these effects produce an artefact at energies $\lesssim 0.02$ a.u. in the right panel of figure 2. Accuracies at the lowest energies can be pushed by increasing both, simulation box size and propagation times.

Figure 3 shows total photoelectron spectra from helium at 200 and 400 nm wavelengths. The exact laser parameters are indicated in the figure captions. At 200 nm ($\omega = 0.228$ a.u.), the ionization threshold is four photons. A single ionic state calculation produces spectra that are 10% accurate with respect to a full dimensional calculation. Addition of second and third shell ionic states improves the accuracy of the spectra to few percent level in the important regions of the spectrum. At 400 nm ($\omega = 0.114$ a.u.), the ionization threshold is eight photons. Also here, a single ionic state computation produces spectra that are 10% accurate with respect to a full dimensional calculation. Addition of more ionic states, does not improve the accuracy further. This is possibly due to the missing continuum of the second electron that is needed to fully describe the polarization of the ionic core.

At longer wavelengths, we find that single ionic state computations are sufficient to produce spectra accurate on the level of 10%. This is consistent with the knowledge that at longer wavelengths, it is the ionization

Table 1. Energies of the used single ionic states of beryllium relative to the ground state ion. The COLUMBUS [21] ionic states are computed at MR-CISD level with aug-cc-pvtz basis.

Ionic state	NIST database (eV)	Columbus energies (eV)
$1s^2 2s$	0.0	0.0
$1s^2 2p$	3.9586	3.9767
$1s^2 3s$	10.9393	10.9851
$1s^2 3p$	11.9638	12.1407
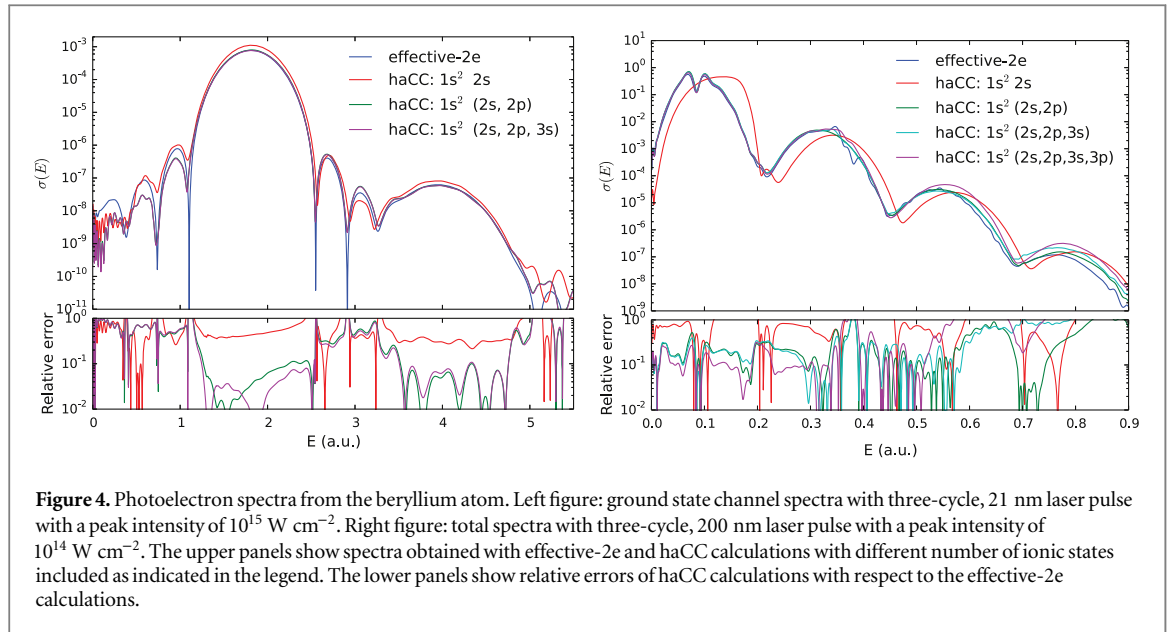
Figure 4. Photoelectron spectra from the beryllium atom. Left figure: ground state channel spectra with three-cycle, 21 nm laser pulse with a peak intensity of 10^{15} W cm^{-2}. Right figure: total spectra with three-cycle, 200 nm laser pulse with a peak intensity of 10^{14} W cm^{-2}. The upper panels show spectra obtained with effective-2e and haCC calculations with different number of ionic states included as indicated in the legend. The lower panels show relative errors of haCC calculations with respect to the effective-2e calculations.

thresholds that play a more important role in determining the ionization yields compared to the exact electronic structure. Our findings show that helium at long wavelengths can be approximated as a single channel system.
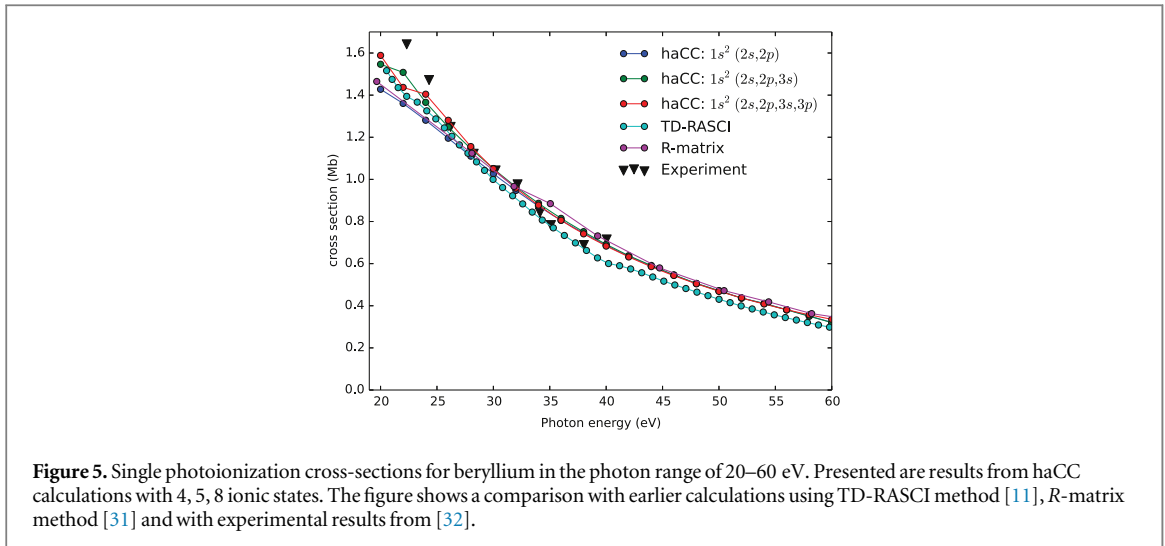
4.2. Beryllium

Beryllium is a four electron system that is often treated as a two electron system due to the strong binding of its inner two electrons. The third ionization potential of beryllium is 153.8961 eV [29]. With photon energies below this third ionization potential, it can be safely treated as an effective two electron system. This allows us to have a benchmark for our spectra by adapting the simple Coulomb potential to an effective potential in our two electron code. We use the effective potential given in [6] for our benchmark calculations. We refer to these as 'effective-2e' calculations.

Table 1 lists the energies of the first 8 ionic states of beryllium relative to the ground ionic state. As the ionic excitation energies are much smaller than in Helium one would expect inter-channel couplings to play a greater role.

Figure 4 shows photoelectron spectra from beryllium with 21 and 200 nm wavelength laser pulses. The exact parameters are indicated in the figure caption. The relative errors of spectra from the haCC calculations are computed with respect to the effective-2e calculations.

At 21 nm, the one and two photon ionization peaks of ground state channel spectra are shown. Here, the single photon ionization process itself needs more than the ground ionic state to produce accurate photoelectron spectra. Adding more ionic states improves the accuracy to a few percent level. We find that the close energetic spacing of beryllium ionic states leads to a greater possibility of inter-channel coupling, which requires more than the ground ionic state to be well represented.

Also, at 200 nm we need more than the ground ionic state to compute realistic spectra. With $1s^2 2s$, $1s^2 2p$ ionic states included, the spectra produced have 20% accuracy with respect to the benchmark calculation. With the addition of $1s^2 3s$ and $1s^2 3p$ states, a structure similar to the one predicted by the benchmark calculation develops around 10 eV. This structure may be identified with the lowest resonance $1s^2 2p 3s$ at 10.71 eV [6]. The coupled channels calculations with the number of ionic states considered here, however do not reproduce the structure on the second peak exactly. This points to a feature of a coupled channels basis that the correct representation of a strongly correlated state that has bound character requires a large number of ionic states. As

Figure 5. Single photoionization cross-sections for beryllium in the photon range of 20–60 eV. Presented are results from haCC calculations with 4, 5, 8 ionic states. The figure shows a comparison with earlier calculations using TD-RASCI method [11], *R*-matrix method [31] and with experimental results from [32].

an alternative strategy, one can explicitly include the correlated state of importance into the basis, if it can be pre-computed, on the same footing as the correlated ground state.

It has been shown through examples in section 4.1 that helium can be modeled as single channel system at longer wavelengths. Lithium, the smallest alkali metal, also has been successfully modeled as a single electron system in an effective potential, for example in [30]. We find that beryllium needs at least two ionic states, $1s^2 2s$ and $1s^2 2p$, for a realistic modeling. It serves as a first simple example where single electron models break down and multiple channels need to be considered.

In figure 5, we present the single photon ionization cross-sections as a function of photon energy from our haCC method and compare them with the cross-sections calculated with TD-RASCI method [11] and *R*-matrix method [31] and with experimental results from [32]. The cross-sections in our time dependent approach are computed using the equation (51) given in [18] with which the N photon ionization cross-section, $\sigma^{(N)}$ in units $\text{cm}^{2N}/\text{s}^{N-1}$ can be computed as:

$$\sigma^{(N)} = (8\pi\alpha)^N \left(\frac{3.5 \times 10^{16}}{I} \right)^N \omega^N \Gamma a_0^{2N} t_0^{N-1}, \tag{42}$$

where I is the intensity in W cm^{-2}, ω is the laser frequency in a.u., α is the fine structure constant and a_0, t_0 are atomic units of length and time respectively. Γ is the total ionization rate which is computed in a time dependent approach by monitoring the rate at which the norm of the wavefunction in a certain inner region drops. As we are computing the rate, the exact size of the inner region does not play a role. The norm drop reaches a steady state irrespective of the inner region size. We used for our computations presented here a 40-cycle continuous wave laser pulse with a three cycle $\cos^2$ ramp up and ramp down and with an intensity of $10^{12} \text{ W cm}^{-2}$. We checked convergence with respect to the pulse duration and the inner region size, and the computations are converged well below the differences seen by addition of ionic states in the basis.

All the theoretical methods agree with each other qualitatively, though there are differences on the level of 5–10% quantitatively. The experimental results from [32] have error bars on the level $\lesssim$10% (0.1 Mb) which are not shown here. All the theoretical results lie in this range except at low energies. In the higher photon energy range, 30–60 eV, the haCC results and the *R*-matrix results are in good agreement compared to the TD-RASCI. In the haCC calculations, including more than 4 ionic states does not change the cross-sections. In the photon energy range 20–30 eV, the haCC computations with 5 and 8 ionic states are in good agreement with TD-RASCI results compared to the *R*-matrix results. In this energy range, the cross-sections from haCC calculations show a dependence on the number of ionic states included. This modulation may be attributed to the presence of auto-ionizing states in this region. Table 3 in [6] presents a list of resonances that appear in beryllium electronic structure. The first ionization potential is 9.3 eV. With photon energies around 20 eV, the resulting photoelectron reaches continuum region where a number of resonances are present. As correlated resonances need many ionic states to be well represented in a coupled channels basis, this may explain the dependence of the cross-section on the number of ionic states in 20–30 eV photon range.

4.3. Hydrogen molecule

The hydrogen molecule in linearly polarized laser fields parallel to the molecular axis, with fixed nuclei has the same symmetry as helium in linearly polarized laser fields. The off-centered nuclear potential, however,
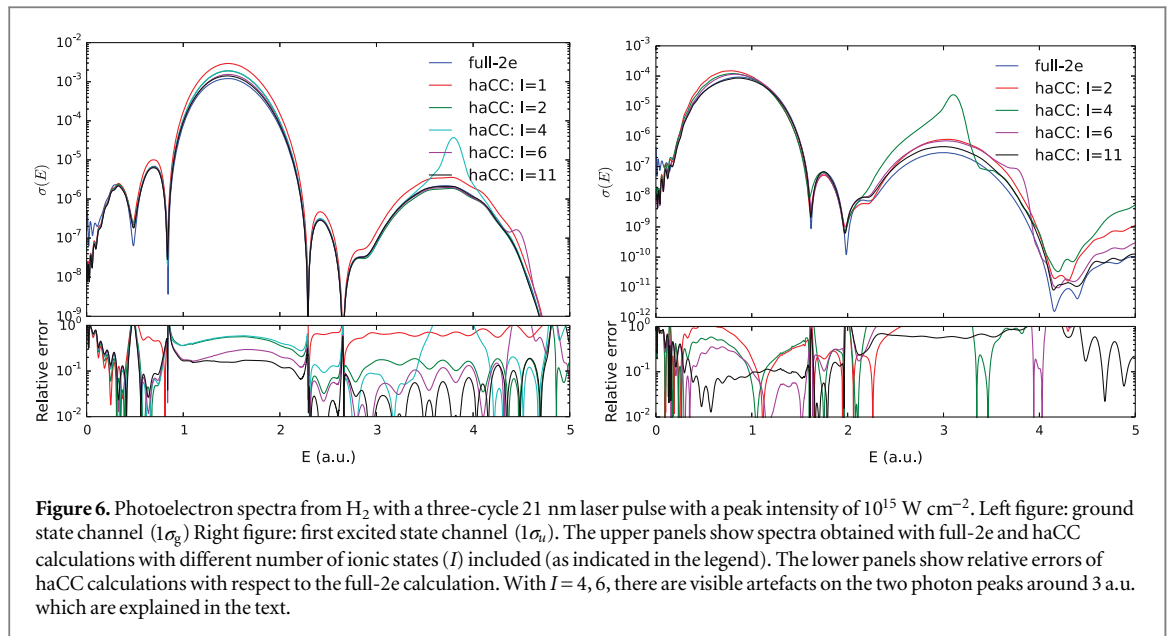
Figure 6. Photoelectron spectra from H_2 with a three-cycle 21 nm laser pulse with a peak intensity of 10^{15} W cm^{-2}. Left figure: ground state channel $(1\sigma_g)$ Right figure: first excited state channel $(1\sigma_u)$. The upper panels show spectra obtained with full-2e and haCC calculations with different number of ionic states (I) included (as indicated in the legend). The lower panels show relative errors of haCC calculations with respect to the full-2e calculation. With $I = 4, 6$, there are visible artefacts on the two photon peaks around 3 a.u. which are explained in the text.

increases the angular momenta requirement when treated with a single center expansion. While the number of basis functions can be reduced through a choice of a more natural coordinate system like prolate spheroidal coordinates for diatomics [33], the challenge of computing two electron integrals remains. In the case of hydrogen molecule at equilibrium internuclear distance ($R_0 = 1.4$ a.u.), a calculation with single center expansion easily converges, as the proton charges do not significantly distort the spherical symmetry of the electron cloud. As a benchmark for spectra, we use results from a full dimensional calculation, that expands the wavefunction in a single center basis.

Figure 6 shows photoelectron spectra from H_2 at 21 nm wavelength. The exact laser parameters are given in the figure caption. The ground state $(1\sigma_g)$ and first excited state $(1\sigma_u)$ channel spectra are shown. We find that, at this wavelength, a single ionic state is not sufficient to produce accurate photoelectron spectra. With the addition of more ionic states, there is a systematic improvement in the accuracy of the calculations. With 11 lowest σ and π ionic states included, we obtain an accuracy of about 10% for the $1\sigma_g$ channel. The single photon ionization to the shake-up channel $1\sigma_u$ is also computed to a few percent accuracy with 11 ionic states. We find that the single ionization continuum of H_2 is more complex than helium and it needs more than a single ionic state.
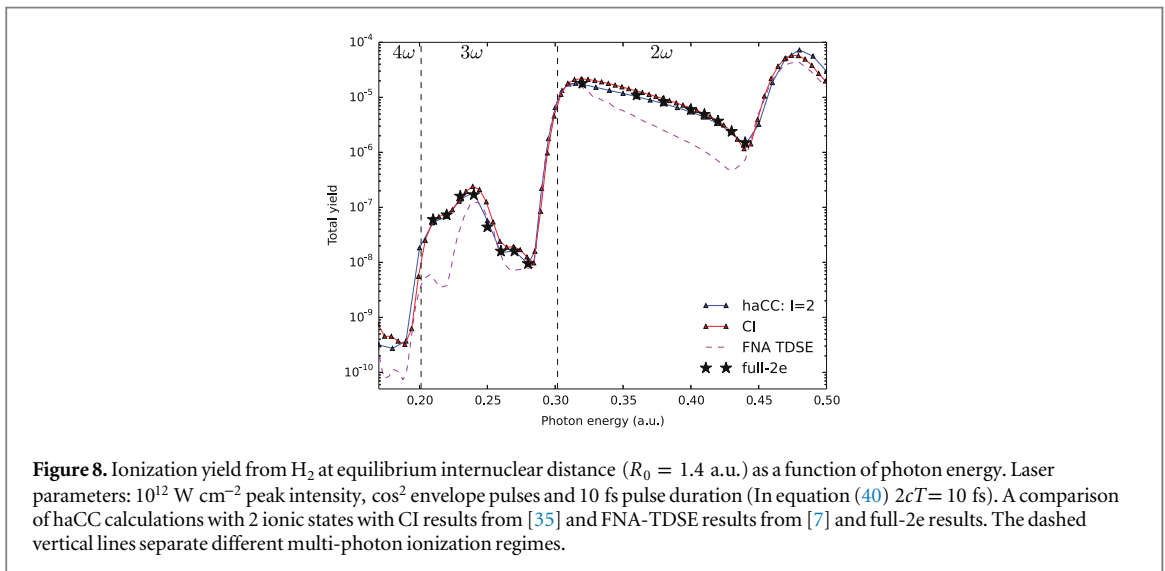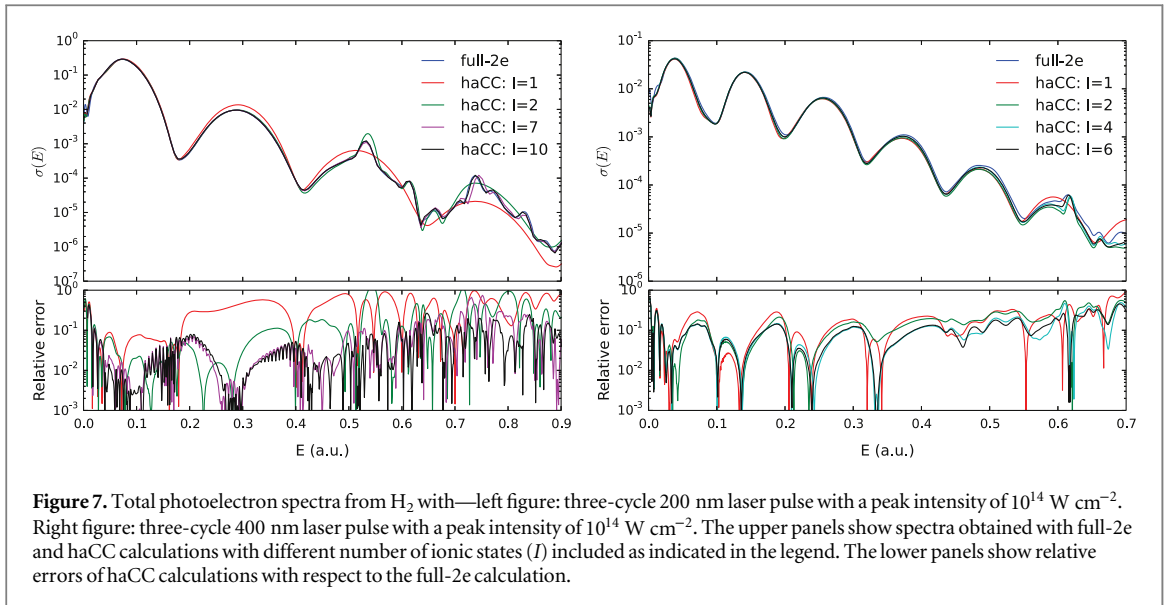
With 4 and 6 ionic states, we find artefacts on the two photon peaks. This is a result of a part of the COLUMBUS neutral ground state $|\mathcal{G}\rangle$ appearing in the eigenvalue spectrum of the Hamiltonian as a spurious doubly excited state $|s\rangle$. Let Π_C be the projector onto the subspace spanned by the coupled-channels basis $\mathcal{A}[|i\rangle|I\rangle]$. Then parts of the correlation contained in $|\mathcal{G}\rangle$ cannot be presented in that basis such that a non-zero correlated state

$$|s\rangle = (1 - \Pi_C)|\mathcal{G}\rangle \neq 0 \tag{43}$$

appears at elevated energies. This spurious correlated state moves to higher energy with addition of ionic states. A straight forward solution to this problem is to compute this state and project it out from the basis. But this would require locating the spurious state in the eigenvalue spectrum, which is very demanding for large Hamiltonians. Fortunately, by their dependence on the number of ionic states, artefacts of this kind are easily detected and can be moved out of the region of interest by using sufficiently many ionic states. Such artefacts are a natural consequence of any ansatz of the kind (5) and need to be monitored.

Figure 7 shows total photoelectron spectra at 200 and 400 nm wavelengths. At 200 nm, spectra are accurate up to 10% with 2 ionic states. Addition of more ionic states helps reproduce additional resonant features in the spectrum. Also at 400 nm, 2 ionic states are sufficient to compute spectra that are accurate on 10% level, except for the resonant features. Inclusion of up to 6 ionic states reproduces the feature around 0.62 a.u. in the 400 nm spectrum, which may be attributed to second or third $^1\Sigma_u^+$ doubly excited state [34]. We find that with H_2 at longer wavelengths, ground ionic state is sufficient to compute realistic spectra and only for resonant features a large number ionic states is required.

Figure 8 shows total ionization yield as a function of photon energy in the range 0.17–0.5 a.u. Results from haCC are compared with data available from other theoretical methods—time-dependent CI method from [35] and FNA-TDSE (fixed nuclei approximation) method from [7]. In addition, several points from our tSURFF-

Figure 7. Total photoelectron spectra from H_2 with—left figure: three-cycle 200 nm laser pulse with a peak intensity of 10^{14} W cm^{-2}. Right figure: three-cycle 400 nm laser pulse with a peak intensity of 10^{14} W cm^{-2}. The upper panels show spectra obtained with full-2e and haCC calculations with different number of ionic states (I) included as indicated in the legend. The lower panels show relative errors of haCC calculations with respect to the full-2e calculation.

Figure 8. Ionization yield from H_2 at equilibrium internuclear distance ($R_0 = 1.4$ a.u.) as a function of photon energy. Laser parameters: 10^{12} W cm^{-2} peak intensity, cos^2 envelope pulses and 10 fs pulse duration (In equation (40) $2cT = 10$ fs). A comparison of haCC calculations with 2 ionic states with CI results from [35] and FNA-TDSE results from [7] and full-2e results. The dashed vertical lines separate different multi-photon ionization regimes.

based full-2e method are included. The haCC calculations shown were performed using two ionic states, convergence was verified by performing four-state calculations at selected points. The vertical lines in the figure separate different multi-photon ionization regimes. The haCC, CI and full-2e are in fair agreement, while FNA-TDSE reproduces the threshold behavior, but severely, by up to an order of magnitude, deviates from the other calculations. The most conspicuous discrepancies between haCC and CI appear in the range $0.3 \sim 0.4$ a.u. where CI exceeds haCC by about 20%. The discrepancies may be a result of the intrinsic limitations or the convergence of either calculation. For example, there are minor discrepancies in the ionization potential: the accurate value at H_2 equilibrium inter-nuclear distance ($R_0 = 1.4$ a.u.) is 0.6045 a.u.(table 1 in [36]),the ionization potential in [35] is 0.590 36 a.u., whereas in our calculations we obtain 0.6034 a.u. Also note that the results in [35] were shifted by 0.0092 a.u. in energy to match the resonance at 0.46 a.u. Although these differences are miniscule for energies they may indicate for somewhat larger deviations in the wave functions and the values of ionization potentials give a measure for the accuracy of the computations. Our full-2e computations that, in principle, could help to resolve the discrepancy are expensive and have not been pushed to an accuracy level which would allow to decide between the two results. However, we believe that the present level of agreement between haCC and CI is quite satisfactory and supports the validity of both approaches.

5. Conclusions

The hybrid anti-symmetrized coupled channels method introduced here opens the route to the reliable *ab initio* calculation of fully differential single photo-emission spectra from atoms and small molecules for a broad range of photon energies. It unites advanced techniques for the solution of the TDSE for one- and two-electron systems in strong fields with state of the art quantum chemistry methods for the accurate description of electronic structure and field-induced bound state dynamics. For the specific implementation we have relied on a finite element description of the strong field dynamics and Gaussian-based CI package of COLUMBUS.

Key ingredients for the successful implementation are good performance of tSURFF for the computation of spectra from comparatively small spatial domains on the one hand and access to the well established technology of quantum chemistry on the other hand. We could obtain the quantum chemical structure in the form of the complete expansion into determinants from COLUMBUS. In future implementations, it may be sufficient to output from a given package the generalized one, two, and three-electron density matrices together with generalized Dyson orbitals, both defined in the present paper. It turned out to be instrumental for accurate results that haCC allows for the inclusion of neutral states in a natural fashion and at very low computational cost.

Several new techniques were introduced and implemented for the establishment of the method. Most notably, the mixed gauge approach [22] turned out to be crucial for being able to take advantage of the field-free electronic structure in presence of a strong field without abandoning the superior numerical properties of a velocity-gauge like calculation. The finite element method used for single-electron strong-field dynamics is convenient, but certainly not the only possible choice. Similar results should be achievable with higher order B-spline methods or any other discretization suitable for solutions of the single electron strong field Schrödinger equation. Low-rank updates are used in several places for the efficient computation of the inverses of the large overlap matrix and to control the linear dependency problems arising from anti-symmetrizing the essentially complete finite elements basis against the Hartree–Fock orbitals.

We have made an effort to explore the potential range of applicability of the method by performing computations in a wide range of parameters on a few representative systems, where results can be checked against essentially complete methods. Spectra for the He atom were independently obtained from fully correlated two-electron calculations. We could demonstrate that haCC gives spectra on the accuracy level 10% with very low effort. An interesting observation is that in the long wavelength regime indeed a single ionization channel produces correct results, justifying *ex post* wide spread model approaches of the strong field community. As a note of caution, we recall that this is only possible as the *fully correlated initial state* is routinely included in the haCC scheme. At short wavelength, the ionic excited state dynamics plays a larger role and reliable results require inclusion of up to 9 ionic channels. With this we could correctly resolve also the peak due to He's doubly excited state.

The second atomic system, Be, was chosen to expose the role of electronic dynamics in the ionic states. While the 1s core electrons are energetically well-separated and no effect of their dynamics was discernable in a comparison with a frozen core model, the narrow spaced ionic states preclude single channel models. Depending on the observable and on desired accuracies, a minimum of two ionic channels had to be used.

For the comparison of H_2 photoionization and photoelectron spectra, we could refer to literature and supplemented the data with full two-electron calculations. At 400 nm, H_2 can be treated as a single channel system. At intermediate wavelengths, we find the need for at least two ionic channels, and we could obtain a fair agreement with comparison data. Here one has to take into consideration that all alternative methods operate near the limits of their applicability.

With this set of results we demonstrated the correctness of the method and its essential features. In our calculations, also the fundamental limitations of the approach were exposed. Clearly, the field-induced dynamics of the ionic part must be describable by a few states with bound character. haCC shares this limitation with any expansion that is limited to a few ionic states. Note that the problem is partly mitigated by the possibility to include fully correlated ground as well as singly- and doubly-excited states with bound-state character that are known to appear in the dynamics.

The method in its present implementation can be applied to many electron atoms [37] and small molecules such as N_2 and CO_2, which will be reported in a forthcoming publication. The ionic states in these molecules are closely spaced as in beryllium and hence they would also need several ionic states in the basis for convergence. We have no reliable heuristics to *a priori* estimate the number of states needed for a given accuracy. From the present experience, we expect that at long wavelengths, for example at 800 nm, inclusion of ionic states in the range of 5–6 eV below the first ionization threshold may be sufficient for convergence. This translates to about 5–6 ionic states in the basis for these systems which is a feasible problem.

At the moment, the computation of the two-electron integrals poses a mild technical limitation for such calculations, and an improvement of the presently rather straight-forward algorithm is needed for going to

larger systems.Treating molecular systems with lower symmetry leads to a further fill in of the Hamiltonian matrix due to the large number of allowed transitions. Such calculations appear quite feasible as well, however at comparatively higher resource consumption than the few hours on a eight-core machine needed for the majority of the results presented here. Another limitation arises when the molecule becomes too large for computing even strong field single-electron dynamics over its complete extension. At present, tSURFF allows us to limit computation boxes to the scale of $\sim$40 a.u. Also, for the single electron part, we use at present single-center expansions, which perform notoriously poorly if scattering centers are distributed over more than a few atomic units. This limitation may well be overcome by a more versatile single-electron discretization, though at significant implementation effort.

Other potential extensions are to double-emission. The tSURFF method was formulated for this situation. Combining such already sizable calculations with a dication described by quantum chemistry in the same spirit as here may be feasible. The formula presented can be readily extended to include that case. However, the scaling is poor such that one may only hope for the simple one- or two-channel situation to be feasible in practice. A cut-down version of such an approach can be used to include non-bound dynamics by describing a second electron's dynamics in a more flexible basis, however, without admitting its emission.

These lines of development will be pursued in forthcoming work.

Acknowledgments

Appendix. Finite element basis

Let $\{r_0, r_1, \ldots, r_n\}$ be points that define n intervals on the radial axis. In a finite element approach, the basis functions $f_i^n(r)$ are chosen such that

$$f_i^n(r) \begin{cases} \neq 0 & \text{if } r \in [r_{n-1}, r_n], \\ = 0 & \text{otherwise.} \end{cases} \tag{A.1}$$

The individual basis functions can be chosen from any complete set, for example, in our case we use scaled Legendre polynomials of typical orders 10–14. Here, we write the finite element index and the function index separately to emphasize that we have two convergence parameters: the order and the number of finite elements. The calculations converge quickly with increasing order compared to with increasing number of elements [38]. The basis functions should also be tailored to satisfy the continuity conditions. This may be accomplished through a transformation on each interval such that the functions satisfy the following conditions:

$$\begin{aligned} f_0^n(r_{n-1}) = 1; \quad & f_0^n(r_n) = 0 \\ f_1^n(r_{n-1}) = 0; \quad & f_1^n(r_n) = 1 \\ f_{i\neq 0,1}^n(r_{n-1}) = 0; \quad & f_{i\neq 0,1}^n(r_n) = 0, \end{aligned} \tag{A.2}$$

Even though we are solving a second order differential equation, it is sufficient to impose just the continuity condition to solve the differential equation. It can be shown through a simple computation, for example as shown in [38], that the matrix elements corresponding to the Laplacian operator can be computed even if the functions are not two times differentiable at the finite element boundaries. This is because the δ-like terms arising due the second derivative are integrated over with continuous functions. The matrices corresponding to various operators in a finite element basis have a banded structure, that can be used to perform various linear algebra operations efficiently.

In a three-dimensional situation with spherical symmetry, these radial finite element functions can be multiplied by a complete set of angular basis functions such as the spherical harmonics to construct a three dimensional basis of the form $f_i^n(r) Y_{lm}(\theta, \phi)$.

References

[1] Meckel M *et al* 2008 Laser-induced electron tunneling and diffraction *Science* **320** 1478–82
[2] Kienberger R *et al* 2004 Atomic transient recorder *Nature* **427** 817–21

[3] Pabst S and Santra R 2013 Strong-field many-body physics and the giant enhancement in the high-harmonic spectrum of xenon *Phys. Rev. Lett.* **111** 233005

[4] Spanner M and Patchkovskii S 2009 One-electron ionization of multielectron systems in strong nonresonant laser fields *Phys. Rev. A* **80** 063411

[5] Jose J, Lucchese R R and Rescigno T N 2014 Interchannel coupling effects in the valence photoionization of SF_6 *J. Chem. Phys.* **140** 204305

[6] Djiokap J M N and Starace A F 2013 Resonant enhancement of the harmonic-generation spectrum of beryllium *Phys. Rev. A* **88** 053412

[7] Palacios A, Bachau H and Martín F 2006 Enhancement and control of H_2 dissociative ionization by femtosecond VUV laser pulses *Phys. Rev. Lett.* **96** 143001

[8] Timmers H, Li Z, Shivaram N, Santra R, Vendrell O and Sandhu A 2014 Coherent electron hole dynamics near a conical intersection *Phys. Rev. Lett.* **113** 113003

[9] Greenman L, Ho P J, Pabst S, Kamarchik E, Mazziotti D A and Santra R 2010 Implementation of the time-dependent configuration-interaction singles method for atomic strong-field processes *Phys. Rev. A* **82** 023406

[10] Caillat J, Zanghellini J, Kitzler M, Koch O, Kreuzer W and Scrinzi A 2005 Correlated multielectron systems in strong laser fields: a multiconfiguration time-dependent Hartree–Fock approach *Phys. Rev. A* **71** 012712

[11] Hochstuhl D and Bonitz M 2012 Time-dependent restricted-active-space configuration-interaction method for the photoionization of many-electron atoms *Phys. Rev. A* **86** 053424

[12] Miyagi H and Madsen L B 2013 Time-dependent restricted-active-space self-consistent-field theory for laser-driven many-electron dynamics *Phys. Rev. A* **87** 062511

[13] Sato T and Ishikawa K L 2013 Time-dependent complete-active-space self-consistent-field method for multielectron dynamics in intense laser fields *Phys. Rev. A* **88** 023402

[14] Miyagi H and Madsen L B 2014 Time-dependent restricted-active-space self-consistent-field theory for laser-driven many-electron dynamics: II. Extended formulation and numerical analysis *Phys. Rev. A* **89** 063416

[15] Bauch S, Sørensen L K and Madsen L B 2014 Time-dependent generalized-active-space configuration-interaction approach to photoionization dynamics of atoms and molecules *Phys. Rev. A* **90** 062508

[16] Haxton D J and McCurdy C W 2015 Two methods for restricted configuration spaces within the multiconfiguration time-dependent Hartree–Fock method *Phys. Rev. A* **91** 012509

[17] Sato T and Ishikawa K L 2015 Time-dependent multiconfiguration self-consistent-field method based on the occupation-restricted multiple-active-space model for multielectron dynamics in intense laser fields *Phys. Rev. A* **91** 023417

[18] Lysaght M A, van der Hart H W and Burke P G 2009 Time-dependent *r*-matrix theory for ultrafast atomic processes *Phys. Rev. A* **79** 053411

[19] Tao L and Scrinzi A 2012 Photo-electron momentum spectra from minimal volumes: the time-dependent surface flux method *New J. Phys.* **14** 013021

[20] Scrinzi A 2012 t-surff: fully differential two-electron photo-emission spectra *New J. Phys.* **14** 085008

[21] Lischka H, Müller T, Szalay P G, Shavitt I, Pitzer R M and Shepard R 2011 Columbus—a program system for advanced multireference theory calculations *WIREs Comput. Mol. Sci.* **1** 191–9

[22] Majety V P, Zielinski A and Scrinzi A 2014 Mixed gauge in strong laser-matter interaction *J. Phys. B: At. Mol. Opt. Phys.* **48** 025601

[23] Scrinzi A 2010 Infinite-range exterior complex scaling as a perfect absorber in time-dependent problems *Phys. Rev. A* **81** 053845

[24] Zielinski A, Majety V P and Scrinzi A 2015 A general solver for the time-dependent schorödinger equation of one and two particle systems, in preparation

[25] Woodbury M 1950 *Inverting Modified Matrices* (*Memorandum Rept., 42, Statistical Research Group*) (Princeton, NJ: Princeton University Press)

[26] Ivanov I A and Kheifets A S 2014 Strong-field ionization of he by elliptically polarized light in attoclock configuration *Phys. Rev. A* **89** 021402

[27] Kaprálová-Žánská P R, Šmydke J and Civiš S 2013 Excitation of helium Rydberg states and doubly excited resonances in strong extreme ultraviolet fields: full-dimensional quantum dynamics using exponentially tempered gaussian basis sets *J. Chem. Phys.* **139** 104314

[28] Scrinzi A and Piraux B 1998 Two-electron atoms in short intense laser pulses *Phys. Rev. A* **58** 1310–21

[29] Drake G W 1988 Theoretical energies for the $n = 1$ and 2 states of the helium isoelectronic sequence up to $z = 100$ *Can. J. Phys.* **66** 586–611

[30] Morishita T and Lin C D 2013 Photoelectron spectra and high Rydberg states of lithium generated by intense lasers in the over-the-barrier ionization regime *Phys. Rev. A* **87** 063405

[31] Berrington K, Quigley L and Zhang H L 1997 The calculation of high-energy photoionization cross sections for the Be isoelectronic sequence *J. Phys. B: At. Mol. Opt. Phys.* **30** 5409

[32] Wehlitz R, Lukić D and Bluett J B 2005 Single and double photoionization of beryllium below 40 eV *Phys. Rev. A* **71** 012707

[33] Vanne Y V and Saenz A 2004 Numerical treatment of diatomic two-electron molecules using a b -spline based ci method *J. Phys. B: At. Mol. Opt. Phys.* **37** 4101

[34] Sánchez I and Martín F 1997 The doubly excited states of the H_2 molecule *J. Chem. Phys.* **106** 7720–30

[35] Förster J, Vanne Y V and Saenz A 2014 Ionization behavior of molecular hydrogen in intense laser fields: Influence of molecular vibration and alignment *Phys. Rev. A* **90** 053424

[36] Lühr A, Vanne Y V and Saenz A 2008 Parameter-free one-center model potential for an effective one-electron description of molecular hydrogen *Phys. Rev. A* **78** 042510

[37] Majety V P and Scrinzi A 2015 Photo-ionization of noble gases: a demonstration of hybrid coupled channels approach *Photonics* **2** 93–103

[38] Scrinzi A and Elander N 1993 A finite element implementation of exterior complex scaling for the accurate determination of resonance energies *J. Chem. Phys.* **98** 3866–75